SCIENCE CHINA
Technological Sciences

• RESEARCH PAPER •

February 2025, Vol. 68, Iss. 2, 1220206:1–1220206:11
https://doi.org/10.1007/s11431-023-2644-7

Broadband low-frequency sound absorption of multifunctional composite metastructure

Yilong YANG[1], Shanshan LIU[3], Yan LI[1,5*], Tong GAO[2], Yongdong PAN[1], Yong LI[3*] & Yabin JIN[1,4,5*]

[1] *School of Aerospace Engineering and Applied Mechanics, Tongji University, Shanghai 200092, China*
[2] *State International Joint Research Center of Aerospace Design and Additive Manufacturing, Northwestern Polytechnical University, Xi'an 710072, China*
[3] *Institute of Acoustics, School of Physics Science and Engineering, Tongji University, Shanghai 200092, China*
[4] *Shanghai Key Laboratory of Intelligent Sensing and Detection Technology, School of Mechanical and Power Engineering, East China University of Science and Technology, Shanghai 200237, China*
[5] *Shanghai Institute of Aircraft Mechanics and Control, Shanghai 200092, China*

Received November 16, 2023; accepted March 22, 2024; published online January 13, 2025

Abstract In this study, we fabricated multifunctional metastructures from carbon fiber-reinforced plastic composites using additive manufacturing technology. These metastructures are characterized by their lightweight, load-bearing capacity, and broadband low-frequency sound absorption properties. The metastructure consists of 36 unit cells, and non-local coupling mechanism was considered for designing the sound absorption performance. We developed an acoustic impedance theory tailored for the metastructure, facilitating an analysis of thermal and viscous dissipation mechanisms. It is proven theoretically and experimentally that the proposed composite metastructure can achieve a noise reduction with an average sound absorption coefficient greater than 0.9 across frequencies in the rage of 330–1500 Hz. We also studied the metastructure's quasi-static and cyclic compression performance, confirming its efficient absorption capabilities after cyclic compression. The proposed design and additive manufacturing method for composite metastructures provides a novel pathway for creating lightweight, multifunctional structures with diverse applications, such as aerospace engineering.

Keywords composite metastructure, broadband sound absorption, additive manufacturing

Citation: Yang Y L, Liu S S, Li Y, et al. Broadband low-frequency sound absorption of multifunctional composite metastructure. Sci China Tech Sci, 2025, 68(2): 1220206, https://doi.org/10.1007/s11431-023-2644-7

1 Introduction

Recently, there has been an urgent demand for lightweight, multifunctional structures within the aerospace and construction industries. Composites are widely used because of their high specific stiffness and strength [1,2]. Designable lightweight composites have become reliable carriers for designing and manufacturing lightweight multifunctional structures. The challenge of mitigating noise, a growing concern for both human health and equipment operation, has become increasingly prominent [3]. Equipment, especially those with large structures, often suffer from low-frequency noise, a problem that is inadequately addressed by traditional sound absorbers owing to their insufficient mechanical performance and limited low-frequency sound absorption capabilities. The development of acoustic metamaterials and metasurfaces has enabled the unprecedented control of sound waves. The design and manufacturing method of combining acoustic metamaterials with composites provides a novel platform for lightweight, multifunctional structures.

Although the mechanical properties of these composites are well-documented, the focus has shifted toward fibrous

* Corresponding author (email: liyan@tongji.edu.cn; yongli@tongji.edu.cn; yabin.jin@ecust.edu.cn)

sound-absorbing materials for noise reduction, exploring both continuous and short fibers [4–7]. Chevillotte and Perrot [8] applied the widely used Johnson-Champoux-Allard (JCA) model to systematically study the effects of channels and pores on the sound absorption performance of porous media and conducted a parametric analysis. Meng et al. [9] studied the acoustic anisotropy of porous sintered metal fiber materials. In the low-frequency range, the samples could not absorb sound, and the working frequency band was mostly concentrated above 1000 Hz. Wu et al. [10] studied the sound-absorption performance of an A356/SiC_p composite foam, demonstrating its narrowband absorption characteristics focused at approximately 1000 Hz. Natural fibers have also been investigated for their sound absorption potential due to their low cost and environmentally friendly nature. Choe et al. [11] studied the acoustic properties of wood-fiber-reinforced polyurethane composite foams for high-frequency sound absorption. Liu et al. [12] used plant-fiber-filled honeycomb sandwich structures to manufacture noise-reducing composites and studied their sound absorption performance; however, their sound absorption did not exhibit a stable low-frequency broadband. Although composites generally exhibit excellent performance in many aspects [13,14], achieving low-frequency broadband noise reduction using composite materials remains a challenge.

These structures and materials cannot achieve low-frequency broadband noise reduction performance. Recently, the development of metamaterials and metasurfaces has provided new solutions for sound absorption [15]. Metamaterials and metasurfaces can achieve physical properties that natural materials do not possess by artificially designing subwavelength structures, and they can modulate acoustic and elastic waves in combination with inverse design methods [16–25]. Many metasurfaces have been proposed for sound absorption, including thin films, curled channels, and local coupling resonators [26–29]. Yang et al. [30] reported that sound waves also follow the causal criterion, and proposed a coupling sound absorber that is close to the optimal thickness of the causal criterion. They used sound-absorbing cotton to weaken the antiresonance phenomenon. Huang et al. [31,32] developed an embedded neck-tube sound absorber that considered viscous and thermal dissipation and proposed a weak resonance non-local coupling mechanism, which significantly reduced the structural thickness. Zhou et al. [33] further proposed the suppression of the over-response and over-damping effects, effectively addressing the antiresonance problem. Combining metastructures with composites provide a solution for designing lightweight, multifunctional structures.

Composites are special materials that must be considered in both the design and manufacturing processes. Traditional composite manufacturing techniques, including autoclave and compression molding, have low molding efficiencies and long processing times. In contrast, additive manufacturing (AM) offers advantages such as lower cost, higher work efficiency, and faster processing times, making it one of the most effective technologies in advanced manufacturing [34,35]. Fused deposition modeling (FDM), a type of AM technology, is widely used in the manufacture of thermoplastic composites. Carbon-fiber-reinforced plastics are used in three-dimensional (3D) printing because of their excellent mechanical properties and designability. Tekinalp et al. [36] used short carbon fiber-reinforced plastics for FDM manufacturing and compared it with the compression molding technology. The tensile strength and modulus of 3D printed samples were improved. Yang et al. [37] conducted the first experimental study on fiber flow and voids during the 3D printing of short fiber-reinforced thermoplastic composites. In terms of metastructure, Mizukami et al. [38–40] used FDM technology to manufacture the local resonance metastructure by combining short carbon fiber-reinforced nylon and continuous carbon fiber-reinforced nylon. They used an inertial amplification mechanism to design and manufacture various composite metastructures to suppress vibrations. Given its ability to manufacture complex periodic metastructures, AM technology holds great promise for the design and manufacturing of multifunctional composite metastructures that integrate load-bearing and noise reduction capabilities.

2 Theory

In this section, we first introduce the theory used for the acoustic absorption calculations and then introduce a compact broadband sound absorption metastructure based on a non-local coupling mechanism. Finally, the causal criterion is employed to demonstrate that the proposed structural thickness of our design is close to the optimal causal thickness.

2.1 Acoustic impedance model

Our proposed multifunctional metastructure comprises 36 unit cells. To assess sound absorption, we initially analyzed the acoustic performance of the unit cell before evaluating the acoustic performance of the overall metastructure. As shown in Figure 1(a), the metastructure is a double-layer square honeycomb structure. Both the top and middle panels of this honeycomb structure were microperforated. The length and width of the metastructure were both L_1 and the height was H. Sound waves incident on the metastructure were reflected after being dissipated by it. The compact square honeycomb exhibited excellent load-bearing and impact energy-absorption performances [41]. The area enclosed by the red dashed line in Figure 1(a) represents the

unit cell of the metastructure. In Figure 1(b), the unit cell of the metastructure consists of top, middle, and bottom panels (orange) and two cavities (yellow). The heights of the cavities were H_1 and H_2, respectively. The thicknesses of the top, middle, and bottom panels were t_1, t_2, and t_3, respectively. The length and width of the unit cell were both A_1. Figure 1 (c) shows the cross-sectional view of a unit cell, where the gray part represents air. The diameters of the micropores shown in the top and middle panels were d_1 and d_2, respectively. The wall thickness of the cavity was fixed, and the length and width inside the cavity were both l_1. The diameters of the two micropores and heights of the two cavities in each unit cell were different, whereas the other geometric parameters were the same.

The sound absorption performance can be characterized by the acoustic impedance, and the boundary of the metastructure can be considered a hard boundary. Therefore, the analysis of the metastructure's acoustic impedance focused solely on the air contained within. The time dependency of this study is $e^{j\omega t}$. The normal incidence absorption coefficient, which is characterized by the surface acoustic impedance of the metastructure, is

$$\alpha = 1 - |r|^2 = 1 - \left|\frac{Z - \rho_0 c_0}{Z + \rho_0 c_0}\right|, \tag{1}$$

where r is the reflection coefficient, Z is the surface acoustic impedance of metastructure, $Z_0 = \rho_0 c_0$ is the characteristic impedance of air, ρ_0 and c_0 are the density and sound velocity of air at room temperature, respectively. Acoustic impedance is defined as p / v, where p is sound pressure and v is particle velocity. We applied transfer matrix theory to calculate the surface acoustic impedance. The sound pressure and velocity relationship between the top and bottom of the air unit cell (Figure 1(d)) is as follows:

$$\begin{bmatrix} P_1 \\ V_1 \end{bmatrix} = T \begin{bmatrix} P_5 \\ V_5 \end{bmatrix}, \tag{2}$$

where T is the transfer matrix.

Acoustic energy is primarily consumed by viscous and thermal dissipation in metastructures. Therefore, in the transfer matrix, we considered the viscous dissipation of micropores and cavities as well as the thermal dissipation of cavities. The reasons for these considerations are discussed in the results and discussion section. For an ideal gas propagating in an irregular tube, the sound pressure and speed

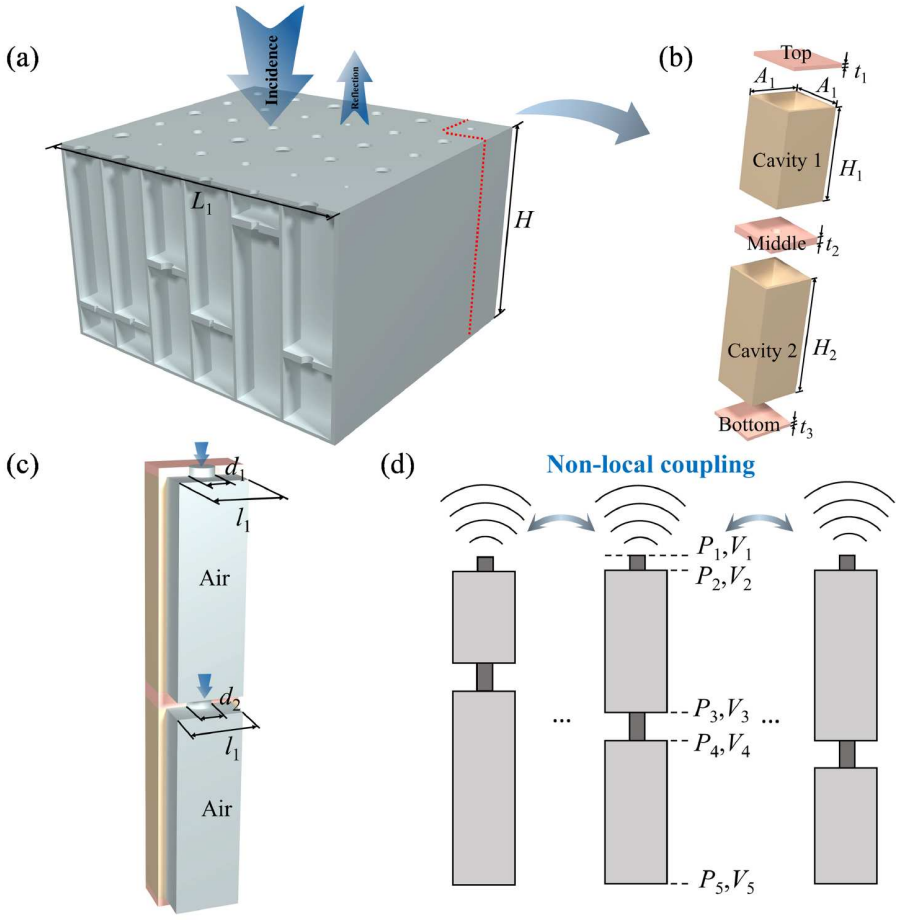

Figure 1 (Color online) Schematic of (a) entire metastructure, (b) unit cell, (c) unit cell with air parts (gray), and (d) non-local coupling mechanism among different unit cells.

can be derived from the motion equation. According to Stinson's derivation [42,43], the sound pressure and speed can be represented by considering the viscous and thermal dissipation through the complex density and complex wavenumber. The complex wavenumber and complex density of the air in the cavity are then represented as

$$\begin{cases} k_c = k\sqrt{\dfrac{\gamma-(\gamma-1)\Psi_h}{\Psi_v}}, \\ \rho_c = \dfrac{\rho_0}{\Psi_v}, \end{cases} \tag{3}$$

where $k = \omega / c_0$ is the acoustic wave number; γ is the specific heat ratio of the air. For complex wavenumber and density, the effects of thermal and viscous dissipation are represented by the thermal and viscosity functions, respectively. The viscous and thermal field functions in the square cavity [31,42,43] are

$$\begin{cases} \Psi_v = {k_v}^2 \sum\limits_{m=0}^{\infty}\left[2\left(\alpha_{mv}m'\right)^{-2}\left(1-\dfrac{\tan\left(l_1\alpha_{mv}/2\right)}{l_1\alpha_{mv}/2}\right)\right], \\ \Psi_h = {k_h}^2 \sum\limits_{m=0}^{\infty}\left[2\left(\alpha_{mh}m'\right)^{-2}\left(1-\dfrac{\tan\left(l_1\alpha_{mh}/2\right)}{l_1\alpha_{mh}/2}\right)\right], \end{cases} \tag{4}$$

where $m' = (m+1/2)\pi, j = \sqrt{-1}$, $\alpha_{mv} = \sqrt{{k_v}^2 - 2m'/l_1}$, $\alpha_{mh} = \sqrt{{k_h}^2 - 2m'/l_1}$, $k_v = -j\omega\rho_0/\eta$ and $k_h = -j\omega\rho_0 C_p/K$ are the viscous and thermal wavenumber, respectively. In the calculations, we retained the first ten terms of the infinite series. In addition, ω is the angular frequency; the dynamic viscosity, thermal conductivity and specific heat at a constant pressure of air are η, K, and C_p, respectively. The thermal and viscous wave numbers in the functions reflect the thermal and viscous dissipation, and the Fourier series in the functions depends on the boundary conditions of the square cross-section. The two-dimensional Fourier series obtained from the boundary conditions can be simplified to a one-dimensional Fourier series [44].

Therefore, the complex characteristic impedance of air is $Z_c = \rho_c c_c = \rho_c \omega / k_c$. When analyzing the impedance of the micropores, the influence of thermal dissipation can be ignored owing to the small thickness of the micropores. Therefore, we used Maa's theory [45] and only the viscous dissipation of the micropores. The acoustic impedance of the micropores is

$$Z_{Mn} = \frac{j\rho_0\omega t_n}{\sigma_n}\left[1-\frac{2J_1\left(\sqrt{-j}y_n\right)}{\sqrt{-j}y_n J_0\left(\sqrt{-j}y_n\right)}\right]^{-1} + \frac{0.85jd_n\rho_0\omega}{\sigma_n} + \frac{\sqrt{2}\eta y_n}{d_n\sigma_n}, \tag{5}$$

where $n = 1, 2$ correspond to the top panel and middle panel respectively, $y_n = d_n\sqrt{\rho_0\omega}/\sqrt{4\eta}$, σ_n is the area ratio of the micropore to the panel in one unit, J_1 and J_2 are first and zero order Bessel functions of the first kind, respectively. Subsequently, based on the continuous conditions of sound pressure and volume velocity, we derived the transfer matrix of the unit cell. The transfer matrix from (P_1, V_1) to (P_2, V_2) is

$$\begin{bmatrix} P_1 \\ V_1 \end{bmatrix} = T_1\begin{bmatrix} P_2 \\ V_2 \end{bmatrix}, \tag{6}$$

$$T_1 = \begin{bmatrix} 1 & Z_{M1} \\ 0 & 1 \end{bmatrix}. \tag{7}$$

The transfer matrix from (P_2, V_2) to (P_3, V_3) is

$$\begin{bmatrix} P_2 \\ V_2 \end{bmatrix} = T_2\begin{bmatrix} P_3 \\ V_3 \end{bmatrix}, \tag{8}$$

$$T_2 = \begin{bmatrix} \cos\left(H_1k_c\right) & j\sin\left(H_1k_c\right)Z_c \\ j\sin\left(H_1k_c\right)/Z_c & \cos\left(H_1k_c\right) \end{bmatrix}. \tag{9}$$

Similarly, the transfer matrices of (P_3, V_3) to (P_4, V_4) and (P_4, V_4) to (P_5, V_5) can be described as

$$\begin{bmatrix} P_3 \\ V_3 \end{bmatrix} = T_3\begin{bmatrix} P_4 \\ V_4 \end{bmatrix}, \tag{10}$$

$$\begin{bmatrix} P_4 \\ V_4 \end{bmatrix} = T_4\begin{bmatrix} P_5 \\ V_5 \end{bmatrix}, \tag{11}$$

$$T_3 = \begin{bmatrix} 1 & Z_{M2} \\ 0 & 1 \end{bmatrix}, \tag{12}$$

$$T_4 = \begin{bmatrix} \cos\left(H_2k_c\right) & j\sin\left(H_2k_c\right)Z_c \\ j\sin\left(H_2k_c\right)/Z_c & \cos\left(H_2k_c\right) \end{bmatrix}. \tag{13}$$

Therefore, the total transfer matrix can be described as

$$T = T_1T_2T_3T_4. \tag{14}$$

Because the boundary of the metastructure is hard, $V_5 = 0$. The surface acoustic impedance of the unit cell is

$$Z_{\text{cell}} = \frac{P_1}{V_1} = \frac{T_{(1,1)}}{T_{(2,1)}}. \tag{15}$$

There are coupling effects among different unit cells in the metastructure [46,47]. We can observe that the surface acoustic impedance of the metastructure is

$$\frac{S}{Z} = \sum_{i=1}^{N}\frac{S_0}{Z_{i\text{cell}}}, \tag{16}$$

where Z is the surface acoustic impedance of the metastructure, $S = L_1L_1$ is the surface area of the metastructure, $Z_{i\text{cell}}$ is the acoustic impedance of the i-th unit cell, S_0 is the surface area of the unit cell, and N is the number of unit cells. Substitute eq. (16) into eq. (1) to obtain the sound absorption coefficient α at angular frequency ω.

2.2 Non-local coupling metastructure

In the previous section, we discussed the coupling effect among unit cells. A schematic diagram of the coupling effect is shown in Figure 1(d). By modulating this coupling effect, we can achieve a non-local coupling effect, which refers to the interference between the reflected waves of a single cell with insufficient sound absorption performance, resulting in the enhancement of the sound absorption performance [32,33]. This coupling mechanism does not rely on modulating the sound absorption performance of individual unit cells but focuses on the coupling effect between unit cells. This coupling mechanism achieves better sound absorption performance by modulating the overall acoustic impedance of the structure. Accordingly, we proposed a compact metastructure with 36 unit cells. Reasonable use of this coupling effect reduces the thickness of the structure.

Genetic algorithms based on MATLAB were used to optimize the acoustic impedance of the overall structure. The aperture and cavity height of each unit cell were set as variables. Because the overall thickness of the structure was constant during optimization, only the height of the required upper cavity was set as a variable. The fitness function of genetic algorithm is

$$W=\sum_{i=0}^{M}\left(\left|\mathrm{Re}\left(Z\left(f_i\right)\right)-1.3\right|+\left|\mathrm{Im}\left(Z\left(f_i\right)\right)-0\right|\right), \tag{17}$$

where M is the number of frequency points and Re and Im are the real and imaginary parts, respectively. When W reached its minimum value, the sound absorption performance of the structure reached its optimal level. In addition, composite design is a special structural design, and manufacturing must be considered. We considered manufacturing constraints in our design and optimization, which are discussed in the results and discussion section.

2.3 Causal optimal thickness

Sound waves belong to the causal wave system, and the incident wave at any time t depends only on the incident wave before time t. The response of sound waves must satisfy the causality principle. The causal principle of sound waves creates an inequality between the absorption spectrum and structural thickness [30]:

$$D\geqslant\frac{1}{4\pi^2\phi}\left|\int_0^{\infty}\ln|1-\alpha(\lambda)|d\lambda\right|=D_{\min}, \tag{18}$$

where D is the thickness of the sample, ϕ is the volume fraction of the sample, λ is the wave length of the sound wave, and $\alpha(\lambda)$ is the absorption coefficient as a function of wavelength. From eq. (18), it can be observed that for any design objective, there is a minimum thickness. Under hard-boundary conditions, the minimum thickness was used as the evaluation standard for the designed metastructure. When $D=D_{\min}$, the designed metastructure is the optimal absorber.

3 Materials and methods

Additive manufacturing technology provides a novel platform for complex metastructure manufacturing. To make the metastructure lightweight and highly load-bearing, we used composite AM technology to manufacture composite metastructure.

This study used short carbon fiber-reinforced nylon composite filaments, specifically Onyx to manufacture composite metastructures through FDM. The Onyx filament, processed using Markforged software, incorporates the short fiber T300 carbon, and PA6 nylon plastic. We used a 3D printer Mark Two (Markforged), as shown in Figure 2(c) to manufacture the composite metastructure. The Eiger software was used for slicing and path planning. Figure 2(a) and (b) show the planning of the printing path and the 3D printing model of the metastructure, respectively. The metastructure had two layers of enclosed cavities and was divided into three parts to facilitate manufacturing. The thickness of the layer is 0.1 mm. Both the top and bottom panels had 10 layers, and the core layer had 620 layers. The accuracy of the holes is much greater than that of the cavities in terms of their impact on the sound absorption performance. As shown in Figure 2(a), due to the manufacturing limitations of FDM technology, the path of the small hole was formed by a circular short fiber wrapped around it. Therefore, the aperture should not be smaller than 1 mm when designing a metastructure. The core layer consisted of two layers of cavities, and we used an Onyx support to manufacture the middle panel. The Onyx supports were manually removed. Owing to the Onyx support, we made the structural design strategy as simple as possible and avoided using structures that are easily damaged. The model of the composite metastructure is shown in Figure 2(d). We used Ergo5882 to bond the top and bottom panels and core layer.

4 Results and discussion

4.1 Sound absorption properties

We optimized and designed a 36 unit cells composite metastructure with a thickness of 64 mm and a cross-section of 99.4 mm × 99.4 mm, considering manufacturing limitations. We conducted standing wave tube experiments to validate the accuracy of the theory and the feasibility of composite AM. The impedance tube, accommodating the 99.4 mm × 99.4 mm composite metastructure, had inner wall dimensions of 100 mm × 100 mm. Figure 3(a) shows a photograph

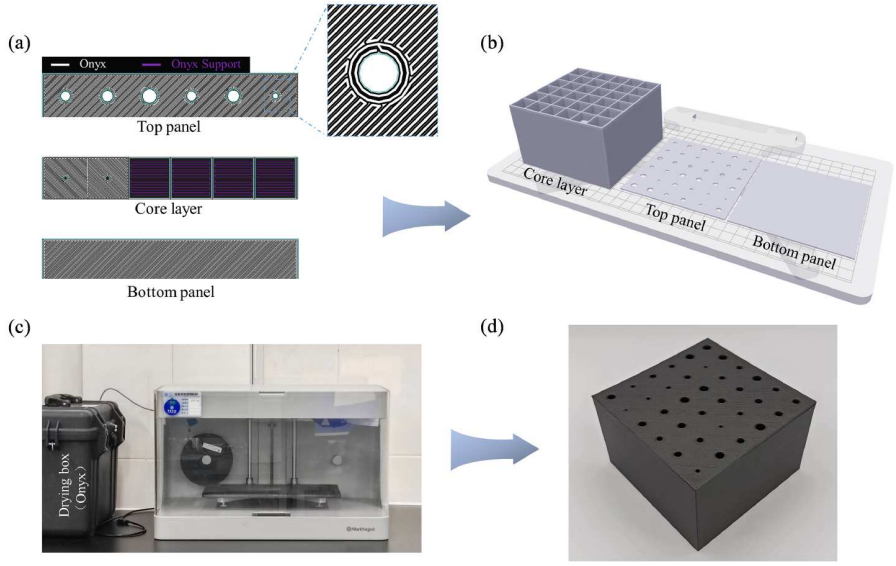

Figure 2 (Color online) (a) Printing path planning strategy of the metastructures; (b) 3D printing model of the metastructure; (c) a photo of 3D printing system; (d) a photo of composite metastructure.

of the impedance tube and other components of the experimental system. A speaker connected to a power amplifier was positioned at one end of the tube while the composite metastructure was placed near the inner wall at the opposite end. A microphone connection acquisition card was used to capture the sound pressure and phase. The experimental system complied with international standard ISO 10534-2. The impedance tube's cut-off frequency is approximately 1700 Hz, with the selected testing range being 300–1500 Hz. For comparison with conventional manufacturing methods for metamaterials, resin samples were manufactured using stereolithography (SLA). The resin used was a DSM8000, and the 3D printer was a Lite 600HD.

As shown in Figure 3(b), it is a comparison diagram of the sound absorption coefficient α and relative acoustic impedance Z/Z_0 between theoretical and experimental results. In the sound absorption coefficient spectrum, the blue solid lines represent the theoretical results, the black dashed lines represent the experimental results for the resin sample, and the gray dotted lines represent the experimental results for the composite sample. The results indicate that the sound absorption curve of the resin sample fits well with the theoretical results and that there are slight differences in the composite sample from 350 to 600 Hz. This is caused by the manufacturing accuracy. SLA technology has a higher accuracy than FDM technology. The line width, layer height, and path of printing materials limit the manufacturing accuracy of FDM technology. The low-frequency region (below 600 Hz) had more resonance modes than the high-frequency region (above 800 Hz); therefore, the low-frequency region was more susceptible to the impact of accuracy in sound absorption design. The theoretical results show that the average sound absorption coefficient is greater than 0.9 from 330 to 1460 Hz. The average sound absorption coefficient of the composite metastructure was greater than 0.9 from 330 to 1500 Hz, and it was almost perfect in the frequency domain greater than 600 Hz. The optimal causal thickness corresponding to the theoretical absorption spectrum was 54 mm. The difference between the composite metastructure and the causal optimal thickness was only 10 mm.

We deduced from eq. (1) that the necessary and sufficient condition for $\alpha = 1$ is $Z/Z_0 = 1$, meaning that the impedance matching condition is the real part value of the relative impedance as 1, and the imaginary part value as 0. In the impedance diagram in Figure 3(b), the solid, dashed, and dotted lines represent the theoretical, resin, and composite samples, respectively. Dark blue represents the real component of relative acoustic impedance, which is the acoustic resistance, whereas red represents the imaginary component of the relative acoustic impedance, which is the acoustic reactance. The research data indicated continuous impedance matching, both theoretically and experimentally, thus validating the accuracy of the theory. Interestingly, the acoustic resistance was slightly greater than 1 in most frequency bands, indicating that the metastructure is an overdamping structure, which is beneficial for reducing the thickness of the structure and making it easier to approach the causal optimal thickness.

To further analyze the sound absorption potential of the metastructure, we conducted a complex frequency plane analysis (Figure 4). Complex frequency analysis involves introducing the imaginary part f_i into the actual frequency f, that is, the complex frequency $F = f + j(f_e + f_i)$, where f_e is

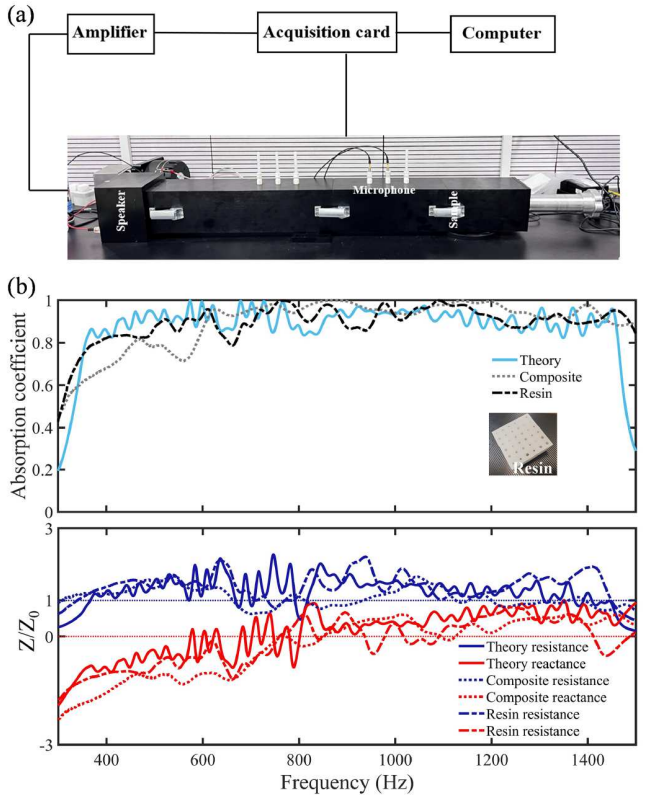

Figure 3 (a) A photo of experimental impedance tube setup. (b) Comparison of the sound absorption curves from theory (blue solid line) and experiments on composite (gray dotted line) and resin (black dashed line) metastructures. The corresponding relative impedance with real part (dark blue) and imaginary part (red).

the inherent dissipation of the system, which can be mathematically characterized by acoustic impedance equations. The imaginary part of the complex frequency represents the gain or loss in the system. Therefore, complex frequency analysis can help predict the acoustic performance of an acoustic system in gain or loss states. The color of the complex frequency plane represents the logarithm of the absolute value of the reflection coefficient. According to eq. (1), the points in Figure 4 that approach yellow are quasi-perfect sound absorption areas (i.e., zero). When $f_i = 0$, the true state of the system is represented. The three thin lines surrounding the area in Figure 4 represent predictions when the sound absorption coefficients were greater than 0.8, 0.85, and 0.9, respectively. When the system is lossless, the zero and pole are symmetrical about the horizontal axis. The additional loss increases or decreases, and this curve moves upward and downward, respectively. Under this inherent loss, the true frequency range surrounded by the thin gray lines is the largest, and moving the curve up or down reduces the working bandwidth. It can be concluded that the sound absorption potential of the metastructure reaches its maximum value at this inherent loss f_e. In addition, the upward

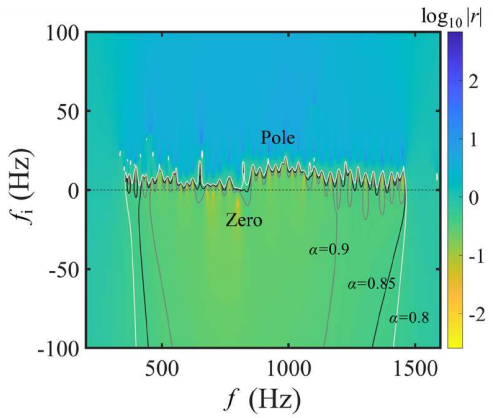

Figure 4 Complex frequency plane illustration of the metastructure, and the three thin lines represent the contour lines for sound absorption coefficients of 0.8, 0.85, and 0.9, respectively.

shift of the zero and pole points in Figure 4 is a result of the increased loss, and most of the zero and pole points are on the same side of the plane. Therefore, the metastructure is in an overdamped state. The overdamping principle brings the thickness closer to the optimal causal thickness [33]. Therefore, the composite metastructure was significantly closer to the causal optimal thickness, even when considering the manufacturing limitations.

To elucidate the sound absorption mechanism, we conducted a simulation analysis of energy dissipation using a multi-physical field simulation. When sound waves propagate in a fluid near a solid wall, viscous and thermal mechanisms primarily account for energy dissipation. Viscous dissipation, which entails energy loss due to friction from molecule diffusion and mutual attraction, causes air velocity to be zero at the wall and increase with distance, leading to a velocity gradient and consequent friction that is converted into thermal energy. Thermal dissipation, or heat transfer due to molecular collisions (also referred to as thermal conduction dissipation), is significant given that solids' thermal conductivities vastly exceed those of fluids, necessitating consideration of losses during thermal conduction. For our analysis, the thermal-viscous-acoustic module was employed to simulate the entire metastructure's dissipation, with non-slip boundary and isothermal conditions as the boundary parameters. We explained that when conducting theoretical calculations, only the viscous dissipation of the hole must be considered without thermal dissipation.

Figure 5(a) and (b) show the nephograms of the viscous and thermal power densities for one cross section of the metastructure. To illustrate the similar dissipation characteristics between low and high frequencies, we selected two absorption frequencies: 600 and 1200 Hz. The colors in the nephogram represent the logarithm of the power density.

In terms of viscous loss, regardless of whether it is 600 or 1200 Hz, the viscous dissipation of the holes was higher than

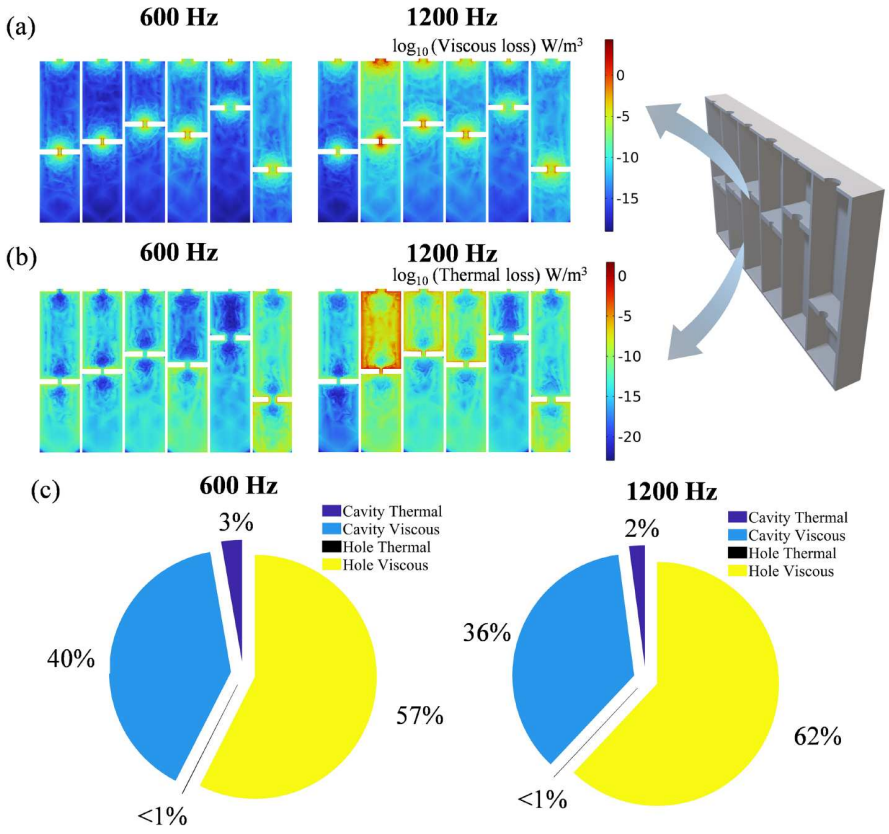

Figure 5 (a) Viscous loss at 600 and 1200 Hz; (b) thermal loss at 600 and 1200 Hz; (c) the proportion of viscous and thermal loss between cavity and hole at 600 and 1200 Hz.

that of the cavities, and energy loss mainly occurred near the inner walls of the holes and cavities. Energy dissipation varies by frequency due to different cavity and hole resonance frequencies, where strong resonance amplifies tangential air velocity, thus increasing viscous power and enhancing sound absorption.

In terms of thermal loss, energy losses were also concentrated on the inner wall. Unlike viscous dissipation, the thermal dissipation of the cavity was greater than that of the hole. Note that the cavity with high viscous dissipation also exhibited significant thermal dissipation since thermal power is directly correlated with external pressure on the thermal boundary layer. High resonance cavities, consequently, had elevated sound pressure.

Figure 5(c) shows the energy-dissipation ratios of the cavities and small holes at 600 and 1200 Hz. The total power of the overall metastructure is

$$Q = Q_M + Q_C = \int_{V_M} E_M \mathrm{d}V_M + \int_{V_C} E_C \mathrm{d}V_C, \tag{19}$$

where Q_M and Q_C are the power of the holes and cavities, respectively, V_M and V_C are the total volumes of the holes and cavities, respectively, and E_M and E_C are the power densities of the holes and cavities, respectively. The specific values of Figure 5(c) are shown in Table 1. We can deduce that viscous dissipation dominated, accounting for approximately 97% to 98% of the total dissipation. The lowest proportion of energy dissipation was the thermal dissipation of the holes, which was less than 1% of the total dissipation. At different frequencies, the proportion of energy dissipation was almost the same. Therefore, in theory, we neglected the thermal dissipation of the holes. However, if the thickness of the hole is large, thermal dissipation cannot be ignored owing to the increase in the area of thermal conduction.

4.2 Mechanical properties

To further verify the mechanical properties of the composite metastructure, quasi-static compression experiments were conducted. Figure 6(a) shows the quasi-static compression process and static rebound of the composite metastructure, and Figure 6(b) shows the load-displacement curve during the compression process. The experimental equipment was a universal testing machine with a load range of 100 kN. The speed of quasi-static compression was 1 mm/min. The composite metastructure was compressed to a deformation rate of 60%, and the photo was taken every 10% deformation (A–F in Figure 6(a) and (b)).

From the load-displacement curve analysis, it is evident

Table 1 Viscous dissipation power and thermal dissipation power of holes and cavities at Case 1 (600 Hz) and Case 2 (1200 Hz)

Components	Case 1 (W)	Case 2 (W)
Cavity thermal	3.11×10^{-7}	2.27×10^{-7}
Cavity viscous	4.50×10^{-6}	3.89×10^{-6}
Hole thermal	6.80×10^{-9}	2.34×10^{-9}
Hole viscous	6.50×10^{-6}	6.72×10^{-6}

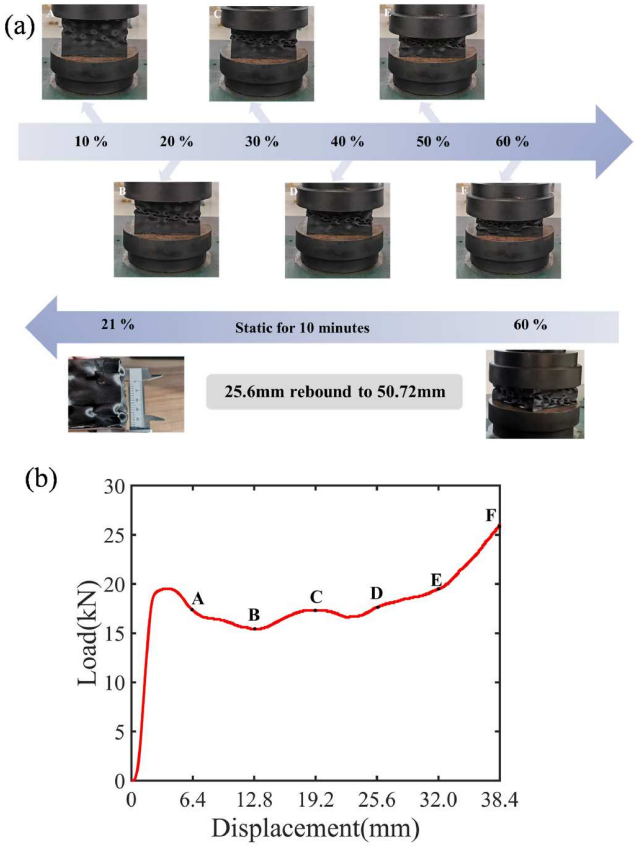

Figure 6 (Color online) (a) Photos of the loading process and the static rebound of composite metastructures; (b) the load-displacement curve of composite metastructure.

that the initial small deformation range exhibited linear elastic mechanical behavior, with the force displacement presenting as a straight line. The elastic limit was reached before point A. Subsequently, the structure entered the plastic yield stage. From point B to point C, the load increased owing to the compaction of the upper cavity folds. From point C to point D, buckling folds appeared in the lower cavity. After point D, the overall metastructure was compacted and the strength gradually increased. After loading at a deformation rate of 60%, we immediately unloaded it. After 10 min of static placement, we measured the overall thickness of the composite metastructure to be 50.72 mm. Moreover, the microcracks generated by ductile fracture can increase the loss of sound energy and enhance sound absorption performance. The compression property of Onyx was better than that of pure nylon. Notably, the bending and tensile properties of the metastructure were significantly enhanced owing to the reinforcement of the carbon fiber. The combination of composites and metastructures provides a new platform for the design and manufacturing of lightweight multifunctional integrated structures.

Cyclic compression experiments were performed to study the cyclic utilization and cyclic loading recovery characteristics of the composite metastructures. The compression speed was 1 mm/min, and five cycles were conducted, with each compression reaching a deformation rate of 20%. The unloading rate was the same as the loading rate. When the deformation rate was 20% each time, it was placed statically for 10 min before proceeding to the next loading. Figure 7 shows the load-displacement curves of the composite metastructure under cyclic loading. The structure has high stiffness at the first cycle, and then the cyclic strength becomes lower and buckling becomes simple. However, each time, the composite metastructure recovered to a deformation rate of less than 8%. The high resilience of this structure was attributed to its nylon matrix. The carbon fibers in this structure provide high-strength mechanical properties. The design and manufacturing of this composite metastructure have broad application prospects in working environments under cyclic loading.

After five compression cycles, the acoustic performances of the samples after static placement were evaluated. Interestingly, the composite metastructure not only restored its original size but also conserved efficient broadband sound absorption performance. Figure 8 shows a comparison of the sound absorption coefficients of the composite metastructure pre and post cyclic compression. The compressed composite metastructure exhibited a significant improvement in sound absorption performance at low-frequencies (400–600 Hz), whereas the sound absorption performance decreased slightly at 800 and 1400 Hz. The compression of the composite metastructure caused a change in the size of the cavity and the shape of the micropores underwent unforeseen changes; however, the boundary conditions did not change. Although the coupling results changed within this frequency band, there was still efficient broadband sound absorption performance. Therefore, the composite metastructure is a reusable noise-reduction structure with a high bearing capacity. Carbon fibers provide better strength and stiffness to the structure, whereas the nylon matrix provides good toughness and acoustic robustness. The lightweight, high-strength, and multifunctional composite metastructure is suitable for multiple industries such as aerospace and construction. Moreover, the design concept of this structure can be extended to sandwich structures with other cores.

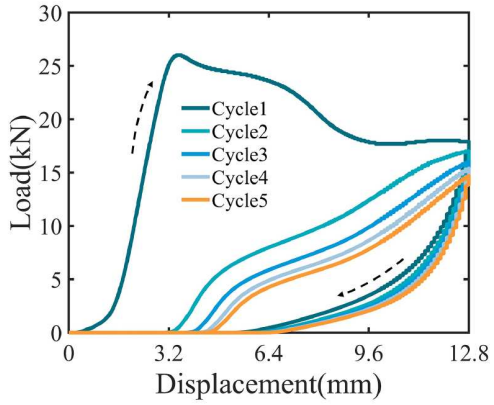

Figure 7 The cyclic compression curve of composite metastructure.

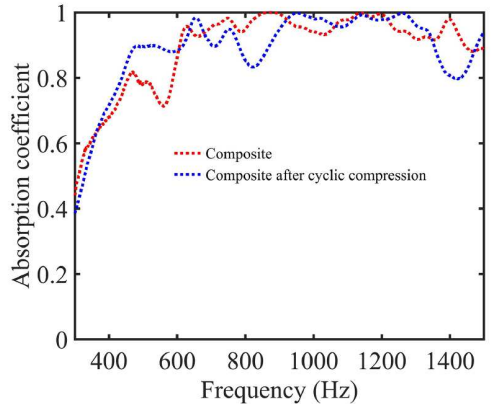

Figure 8 Comparison of sound absorption of composite metastructure before and after cyclic compression.

5 Conclusion

In summary, we proposed a short fiber-reinforced nylon composite metastructure based on AM, developed the acoustic impedance theory of the metastructure, including the thermal dissipation of the cavity, and further analyzed the thermal viscous dissipation mechanism using the finite element method. The constraints of composite additive manufacturing were considered in the design. The metastructure achieves notable noise reduction, with an average sound absorption coefficient greater than 0.9 in the range of 330–1500 Hz, showcasing low-frequency wideband capabilities. The quasi-static compression performance of the structure was studied, and the sound absorption performances of the structure before and after cyclic compression were compared, proving that the structure was reusable. These findings underscore the potential of this approach in developing multifunctional, lightweight composite structures, with a particular focus on continuous-fiber-reinforced composites.

Acknowledgements This work was supported by the National Key R&D Program of China (Grant No. 2022YFB4602000), the National Natural Science Foundation of China (Grant No. 12272267), the Young Elite Scientists Sponsorship Program by CAST (Grant No. 2021QNRC001), Shanghai Science and Technology Committee (Grant Nos. 22JC1404100, 21JC1405600), the Fundamental Research Funds for the Central Universities and the Special Funds of the Tongji University for "Sino-German Cooperation 2.0 Strategy", and Shanghai Gaofeng Project for University Academic Program Development.

References

1 Lubineau G, Rahaman A. A review of strategies for improving the degradation properties of laminated continuous-fiber/epoxy composites with carbon-based nanoreinforcements. Carbon, 2012, 50: 2377–2395
2 Chen Q, Boisse P, Park C H, et al. Intra/inter-ply shear behaviors of continuous fiber reinforced thermoplastic composites in thermoforming processes. Compos Struct, 2011, 93: 1692–1703
3 Cheng X, Chen X, Rong J, et al. Low-frequency noise reduction of rocket fairings using horn-shaped-neck helmholtz resonators. J Spacecr Rockets, 2019, 56: 273–282
4 Cao L, Fu Q, Si Y, et al. Porous materials for sound absorption. Compos Commun, 2018, 10: 25–35
5 Tang X, Yan X. Acoustic energy absorption properties of fibrous materials: A review. Compos Part A-Appl Sci Manuf, 2017, 101: 360–380
6 Yang W D, Li Y. Sound absorption performance of natural fibers and their composites. Sci China Tech Sci, 2012, 55: 2278–2283
7 Lu T J, Kepets M, Dowling A P. Acoustic properties of sintered FeCrAlY foams with open cells (II): Sound attenuation. Sci China Ser E-Technol Sci, 2008, 51: 1812–1837
8 Chevillotte F, Perrot C. Effect of the three-dimensional microstructure on the sound absorption of foams: A parametric study. J Acoust Soc Am, 2017, 142: 1130–1140
9 Meng H, Ao Q B, Ren S W, et al. Anisotropic acoustical properties of sintered fibrous metals. Compos Sci Tech, 2015, 107: 10–17
10 Wu J, Li C, Wang D, et al. Damping and sound absorption properties of particle reinforced Al matrix composite foams. Compos Sci Tech, 2003, 63: 569–574
11 Choe H, Sung G, Kim J H. Chemical treatment of wood fibers to enhance the sound absorption coefficient of flexible polyurethane composite foams. Compos Sci Tech, 2018, 156: 19–27
12 Liu Z, Dong C, Tong L, et al. A pre-screening study of honeycomb sandwich structure filled with green materials for noise reduction. Compos Part A-Appl Sci Manuf, 2022, 163: 107226
13 Wen Z H, Wang D W, Ma L. Sound transmission of composite sandwich panel with face-centered cubic core. Mech Adv Mater Struct, 2019, 28: 1663–1676
14 Chen D, Li J, Ren J. Study on sound absorption property of ramie fiber reinforced poly(l-lactic acid) composites: Morphology and properties. Compos Part A-Appl Sci Manuf, 2010, 41: 1012–1018
15 Jin Y, Pennec Y, Bonello B, et al. Physics of surface vibrational resonances: Pillared phononic crystals, metamaterials, and metasurfaces. Rep Prog Phys, 2021, 84: 086502
16 Jin Y, Kumar R, Poncelet O, et al. Flat acoustics with soft gradient-index metasurfaces. Nat Commun, 2019, 10: 143
17 Liu Z, Zhang X, Mao Y, et al. Locally resonant sonic materials. Science, 2000, 289: 1734–1736
18 Ma G, Yang M, Xiao S, et al. Acoustic metasurface with hybrid resonances. Nat Mater, 2014, 13: 873–878
19 He L, Wen Z, Jin Y, et al. Inverse design of topological metaplates for flexural waves with machine learning. Mater Des, 2021, 199: 109390
20 Jin Y, Zeng S, Wen Z, et al. Deep-subwavelength lightweight metastructures for low-frequency vibration isolation. Mater Des, 2022, 215: 110499
21 Gu T, Wen Z, He L, et al. A lightweight metastructure for simulta-

neous low-frequency broadband sound absorption and vibration isolation. J Acoust Soc Am, 2023, 153: 96–104
22 Li X, Yu X, Zhao M, et al. Multi-level bioinspired microlattice with broadband sound‐absorption capabilities and deformation-tolerant compressive response. Adv Funct Mater, 2022, 33: 2210160
23 Li X, Yu X, Chua J W, et al. Microlattice metamaterials with simultaneous superior acoustic and mechanical energy absorption. Small, 2021, 17: e2100336
24 Li X, Xiao R, Chen J Z, et al. Plate-based cylinder metamaterial with negative Poisson's ratio and outstanding mechanical performance. Sci China Tech Sci, 2023, 66: 793–806
25 Chen K K, Tu G W, Dong X J, et al. Multifunctional application of nonlinear metamaterial with two-dimensional bandgap. Sci China Tech Sci, 2023, 66: 869–880
26 Tang Y, Li F, Xin F, et al. Heterogeneously perforated honeycomb-corrugation hybrid sandwich panel as sound absorber. Mater Des, 2017, 134: 502–512
27 Wang D W, Wen Z H, Glorieux C, et al. Sound absorption of face-centered cubic sandwich structure with micro-perforations. Mater Des, 2020, 186: 108344
28 Jin Y, Yang Y, Wen Z, et al. Lightweight sound-absorbing metastructures with perforated fish-belly panels. Int J Mech Sci, 2022, 226: 107396
29 Qu S, Sheng P. Microwave and acoustic absorption metamaterials. Phys Rev Appl, 2022, 17: 047001
30 Yang M, Chen S, Fu C, et al. Optimal sound-absorbing structures. Mater Horiz, 2017, 4: 673–680
31 Huang S, Fang X, Wang X, et al. Acoustic perfect absorbers via Helmholtz resonators with embedded apertures. J Acoust Soc Am, 2019, 145: 254–262
32 Huang S, Zhou Z, Li D, et al. Compact broadband acoustic sink with coherently coupled weak resonances. Sci Bull, 2020, 65: 373–379
33 Zhou Z, Huang S, Li D, et al. Broadband impedance modulation via non-local acoustic metamaterials. Natl Sci Rev, 2022, 9: nwab171
34 Yang Z, Fu K, Zhang Z, et al. Topology optimization of 3D-printed continuous fiber-reinforced composites considering manufacturability. Compos Sci Tech, 2022, 230: 109727
35 Zhang Z, Long Y, Yang Z, et al. An investigation into printing pressure of 3D printed continuous carbon fiber reinforced composites. Compos Part A-Appl Sci Manuf, 2022, 162: 107162
36 Tekinalp H L, Kunc V, Velez-Garcia G M, et al. Highly oriented carbon fiber-polymer composites via additive manufacturing. Compos Sci Tech, 2014, 105: 144–150
37 Yang D, Zhang H, Wu J, et al. Fibre flow and void formation in 3D printing of short-fibre reinforced thermoplastic composites: An experimental benchmark exercise. Addit Manuf, 2021, 37: 101686
38 Mizukami K, Funaba K, Ogi K. Design and three-dimensional printing of carbon-fiber-composite elastic metamaterials with inertial amplification mechanisms. J Sound Vib, 2021, 513: 116412
39 Mizukami K, Kawaguchi T, Ogi K, et al. Three-dimensional printing of locally resonant carbon-fiber composite metastructures for attenuation of broadband vibration. Compos Struct, 2021, 255: 112949
40 Mizukami K, Kumamoto Y. 3D printing of fiber composite sandwich metamaterial with spiral resonators for attenuation of low-frequency structural vibration. Compos Part A-Appl Sci Manuf, 2023, 172: 107594
41 Duan S, Tao Y, Lei H, et al. Enhanced out-of-plane compressive strength and energy absorption of 3D printed square and hexagonal honeycombs with variable-thickness cell edges. Extreme Mech Lett, 2018, 18: 9–18
42 Stinson M R. The propagation of plane sound waves in narrow and wide circular tubes, and generalization to uniform tubes of arbitrary cross-sectional shape. J Acoust Soc Am, 1991, 89: 550–558
43 Stinson M R, Champoux Y. Propagation of sound and the assignment of shape factors in model porous materials having simple pore geometries. J Acoust Soc Am, 1992, 91: 685–695
44 Kozlov V F, Fedorov A V, Malmuth N D. Acoustic properties of rarefied gases inside pores of simple geometries. J Acoust Soc Am, 2005, 117: 3402–3411
45 Maa D Y. Potential of microperforated panel absorber. J Acoust Soc Am, 1998, 104: 2861–2866
46 Romero-García V, Theocharis G, Richoux O, et al. Use of complex frequency plane to design broadband and sub-wavelength absorbers. J Acoust Soc Am, 2016, 139: 3395–3403
47 Krushynska A O. Between science and art: Thin sound absorbers inspired by Slavic ornaments. Front Mater, 2019, 6: 182